A diffusion model for liquid metal dealloying. Application to NiCu precursors dealloyed in liquid Ag

Louis Lesage, Takumi Suga, Takeshi Wada, Hidemi Kato, Christophe Le Bourlot, Eric Maire, Nicolas Mary, Pierre-Antoine Geslin

Acta Materialia 272 (2024) 119908

Contents lists available at ScienceDirect

Acta Materialia

journal homepage: www.elsevier.com/locate/actamat

Full length article

A diffusion model for liquid metal dealloying. Application to NiCu precursors dealloyed in liquid Ag

Louis Lesage [a,b,c,*], Takumi Suga [b], Takeshi Wada [d], Hidemi Kato [c,d], Christophe Le Bourlot [a], Eric Maire [a], Nicolas Mary [a,c], Pierre-Antoine Geslin [a,**]

[a] CNRS, INSA Lyon, Universite Claude Bernard Lyon 1, MATEIS, UMR 5510, Villeurbanne Cedex, 69621, France
[b] Department of Materials Science, Graduate School of Engineering, Tohoku University, Sendai, 980-8579, Japan
[c] ELyTMaX IRL3757, CNRS, Univ Lyon, INSA Lyon, Centrale Lyon, Universite Claude Bernard Lyon 1, Tohoku University, Sendai, 980-8577, Japan
[d] Institute for Materials Research, Tohoku University, Sendai, 980-8577, Japan

ARTICLE INFO

Keywords:
Dealloying
Porous materials
Diffusion models
Thermodynamical equilibria

ABSTRACT

Liquid metal dealloying is a promising technique to elaborate porous metallic materials with potential applications for catalysis and energy storage. It consists in the selective dissolution of an element out of a precursor alloy by immersing it in a liquid bath. To model this process, we introduce a one-dimensional diffusion model that relies on the thermodynamic properties of the ternary system, and on a maximum velocity criterion of the reaction front. The model is compared to experimental measurements conducted on NiCu samples dealloyed in liquid Ag. Regarding the kinetics, the model enables to reach experimental time-scales, replicate experimental trends, and reveal the influence of the ligament structure on the dealloying rate. Also, by assuming thermodynamic equilibria between solid and liquid phases in the dealloyed region, the microstructure gradient obtained numerically is in satisfactory agreement with experimental measurements. These numerical results are obtained without adjustable parameters, which opens the possibility to predict dealloyed microstructures as function of the process parameters (precursor and bath composition, dealloying time and temperature, etc.).

1. Introduction

Porous materials have been attracting increasing attention, may it be for their applications as catalysts [1,2] or for energy storage [3,4] that both require an open porosity with a large specific surface to maximize the exchange and reaction area. Dealloying emerged as a promising manufacturing technique for the elaboration of these structured materials. It is based on the selective dissolution of an alloying element from a precursor alloy, resulting in the reorganization of the material into a porous structure. Among the various dealloying techniques (electrochemical dealloying [5,6], vacuum dealloying [7], molten salt dealloying [8]...), the present study focuses on liquid metal dealloying (LMD), which presents the advantage of being applicable to a wide range of metals (Ni, Fe, Cr, Ta, Ti...). LMD has been brought to light in 2011 by Wada et al. [9] and consists in immersing an AB precursor alloy into a liquid metal C with A and B respectively immiscible and miscible into C. Upon the dissolution of B in C, A reorganizes into a fine porous structure that coarsens after its formation [10,11]. In a second step, the phase containing B and C can be removed by chemical etching.

The development of LMD requires predictive models for the dealloying kinetics and the resulting morphology in order to optimize the resulting microstructures and morphologies (i.e. the composition and size of ligaments). LMD shows similarities with solidification processes, as it involves diffusion of species at high temperatures and the motion of solid/liquid interfaces.

As in solidification, equilibrium thermodynamics can serve as a general framework for the prediction of the microstructure obtained from LMD. For example, Wada et al. [12] showed that changing thermodynamic equilibria by modifying the bath composition allowed a control of the ligament composition and a modification of the dealloying kinetics. Thermodynamics is also at the basis of the development of phase field models that contributed to unveil the formation and coarsening processes at play during LMD [11,13–16]. The phase field results from these studies highlight the dependence of the dealloying pattern

* Corresponding author at: CNRS, INSA Lyon, Universite Claude Bernard Lyon 1, MATEIS, UMR 5510, Villeurbanne Cedex, 69621, France.
** Corresponding author.
E-mail addresses: louis.lesage@insa-lyon.fr (L. Lesage), pierre-antoine.geslin@insa-lyon.fr (P.-A. Geslin).

https://doi.org/10.1016/j.actamat.2024.119908
Received 19 December 2023; Received in revised form 29 March 2024; Accepted 7 April 2024
Available online 9 April 2024

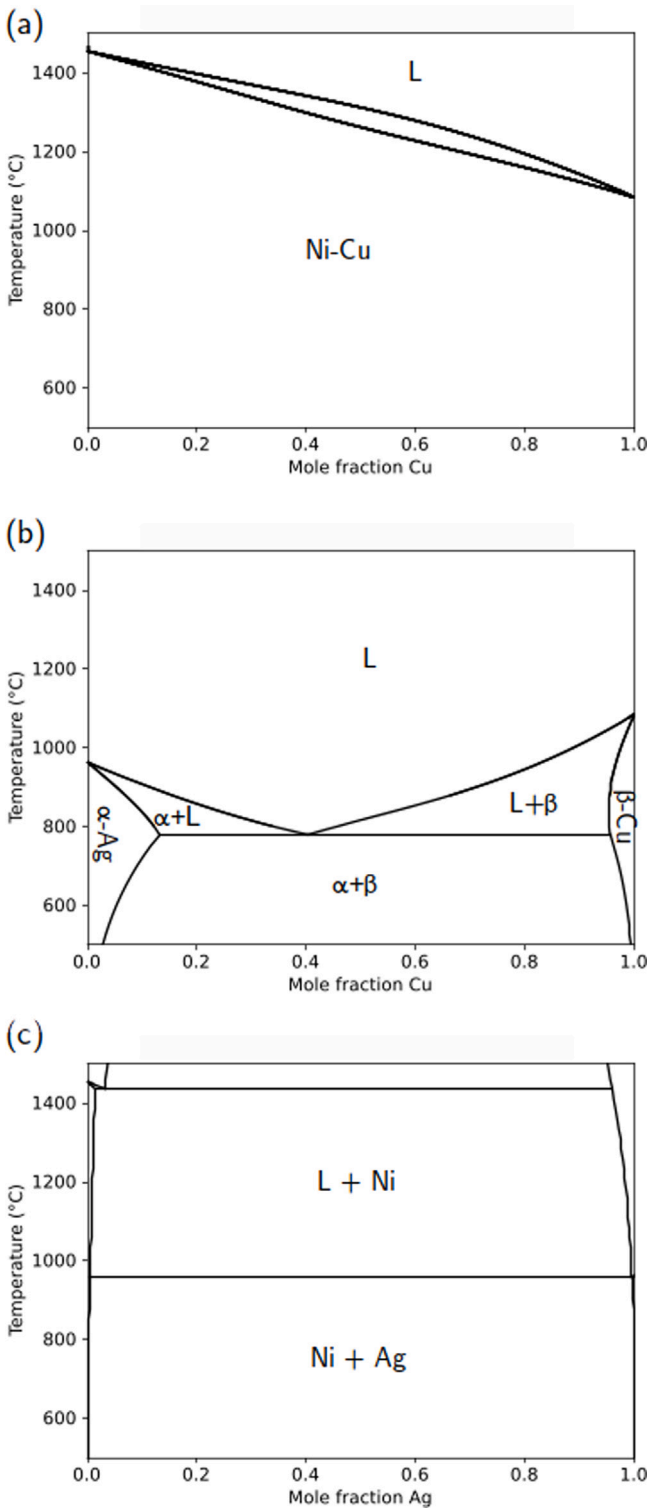

Fig. 1. Binary phase diagrams between 500 °C and 1500 °C: (a) Ni–Cu. (b) Ag–Cu. (c) Ni–Ag. [17].

formation on the different dealloying parameters (precursor composition, temperature, dealloying time, etc.). Recent developments [14–16] allowed to understand the mechanisms affecting the dealloying rate and ligaments morphology, such as solid state diffusivity, the leakage of the targeted element (A) in the bath and the influence of grain boundaries on the dealloyed morphology.

While phase field modelling offers a powerful physics-based tool to model LMD, it also suffers from some limitations. The energies of the different phases are calibrated from thermodynamic data [18] but how these energies interpolate in the interfacial regions depends on the model formulation [19–22]. The control of the interfacial energy and its dependence on the interfacial compositions requires a special care that has been overlooked in the model formulations used for LMD [13–15], resulting in possible artifacts. More importantly, the simulated volumes are of the order a few μm at most, and reaching experimental time and length-scales with phase field approaches would require out-of-reach computational resources. Hence, phase field results are often extrapolated over several decades to be compared to experimental measurements [13,14].

An alternative to phase field modelling is to treat dealloying as a simple 1D diffusion-limited problem as done in Refs. [23,24]; this approach seems reasonable because the dealloying process is controlled by the diffusion of the sacrificial element in the bath. Even though these diffusion models showed satisfying results for composition profiles in the liquid, they are based on several simplistic assumptions incompatible with experimental observations and phase field results. Indeed, the model does not take into account the obstruction of diffusion by ligaments during the dealloying process and considers that the ligaments composition is fixed from the onset of their formation which contradicts experimental [25] and simulation [13,14] results. Moreover, the equilibrium condition chosen at the interface is based on experimental measurements and does not evolve with time, whereas phase field simulations showed that the compositions at the dealloying front evolve during dealloying [14]. Finally, the diffusion is treated as in a binary system and the model neglects the diffusion of the target element in the bath, which has been shown to play a role [15]. This highlights the necessity to treat LMD as a ternary diffusion problem.

In this work, we develop diffusion models with a more complete integration of the thermodynamics of the ternary system, and relaxing the assumptions mentioned above. In particular, we incorporate the influence of the ligament structure that impedes the diffusion of the sacrificial element away from the dealloying front. We focus on the dealloying of NiCu precursors in pure Ag bath [26], that is considered as a model system for liquid metal dealloying because of the simplicity of its phase diagram. The paper is organized as follows: in Section 2, we first introduce the thermodynamics of the NiCuAg system under investigation. Next, Section 3 describes the dealloying experiments conducted on this system and the methods used to characterize the microstructure of the samples. Section 4 is dedicated to the description of the diffusion model. In particular, the analytical solutions described in 4.1 and their comparisons with experimental measurements show the necessity to incorporate a maximum velocity criterion to select the appropriate equilibrium at the reaction layer. In 4.2, this criterion is used in a numerical model that relaxes the approximations of the analytical treatment. Section 5 is dedicated to discuss the model's results and their comparison with experimental measurements regarding kinetics, interface composition and composition profiles in the dealloyed region.

2. System under study: NiCu dealloyed in Ag bath

In this work, we choose to focus on the dealloying of NiCu samples in Ag liquid; Ni being the target element, Cu the sacrificial element dissolving in the Ag bath. This system holds the advantage of being well assessed thermodynamically [17,27–29]. The three binary phase diagrams of the system are shown in Fig. 1. Ni–Cu alloys form homogeneous FCC solid solution over a large range of compositions and temperatures, facilitating the elaboration of solid solution precursor samples (see Fig. 1.a). Fig. 1.b and c also highlight the large miscibility of Cu in liquid Ag at this temperature and the immiscibility of Ni in liquid Ag, two properties that enable the dealloying reaction by promoting (respectively preventing) the dissolution of Cu (resp. Ni) in Ag. Because of the melting temperature of silver and copper (T_m^{Ag} =

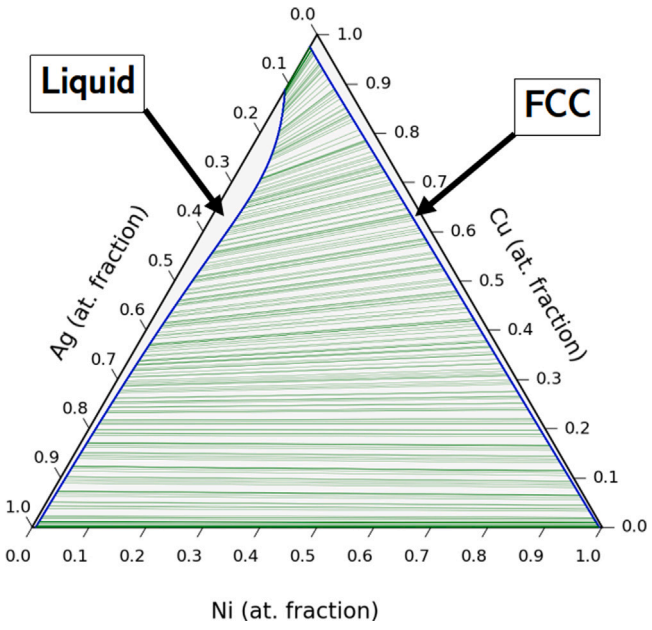

Fig. 2. Ternary NiCuAg phase diagram at 1000 °C [17].

961 °C and T_m^{Cu} = 1085 °C), the target temperature for dealloying is fixed at 1000 °C, therefore promoting the dissolution of Cu in the liquid Ag bath without melting the NiCu precursor alloy.

In addition, the ternary NiCuAg system has also been thoroughly assessed by Liu et al. [17]. Their assessment relies on quantitative comparison with experimental measurements performed at temperatures ranging from 800 °C and 1400 °C. The thermodynamic parameters provided in Ref. [17] enable to reliably calculate the phase diagram at 1000 °C which is represented in Fig. 2. It displays a series of equilibria (represented with green tie-lines) between face-centred cubic (FCC) NiCu solid solutions and Ag rich liquids. In particular, the phase diagram reveals the simplicity of the system's thermodynamics at this temperature, that does not involve the formation of intermetallic phases nor the development of 3-phases equilibria. The simplicity of the system as well as the detailed assessment of its thermodynamics make it an ideal candidate to compare experimental measurements with predictions of modelling tools.

The dealloying kinetics being mostly controlled by the diffusion of Cu in liquid Ag, the diffusion coefficient $D^{(l)}_{Cu\to Ag}$ originally assessed by Yamamura *et al.* [30–32] is an important input of the model: the activation energy of the diffusive process was determined to be Q = 42 kJ/mol and the pre-exponential constant $D_0 = 1.2\times10^5\ \mu m^2/s$. The relation $D^{(l)}_{Cu\to Ag} = D_0\ \exp\left(\frac{-Q}{RT}\right)$ yields a diffusion coefficient $D^{(l)}_{Cu\to Ag}$ = 2300 $\mu m^2/s$ at 1000 °C.

On the other hand, the diffusion coefficient of Ni in liquid Ag has not been carefully assessed in the literature. For simplicity reasons, and after confirming that variations of $D^{(l)}_{Ni\to Ag}$ had a minor influence on the numerical results, we will consider a unique diffusion coefficient in the liquid phase $D_l = D^{(l)}_{Ni\to Ag} = D^{(l)}_{Cu\to Ag}$.

3. Dealloying experiments

Dealloying experiments were performed with precursors $Ni_{50}Cu_{50}$ and $Ni_{20}Cu_{80}$ alloys elaborated by arc-melting from pure Cu (99.99 wt%) and Ni (99.95 wt%) and casting. These precursor alloys were cut in cylinders (diameter 10 mm, thickness 0.8–2 mm).

After reaching a vacuum of 4×10^{-3} Pa and filling the atmosphere with He up to a pressure of 0.5 bar, Ag was melted by inductive heating in a carbon crucible. Once the targeted temperature was reached, the precursor alloys were immersed in liquid Ag. The bath was chosen to be large compared to the precursor sample such that the latter represents less than 3 at.% of the entire system. Dealloying was performed at 1000 °C for immersion times ranging from 25 to 300 s.

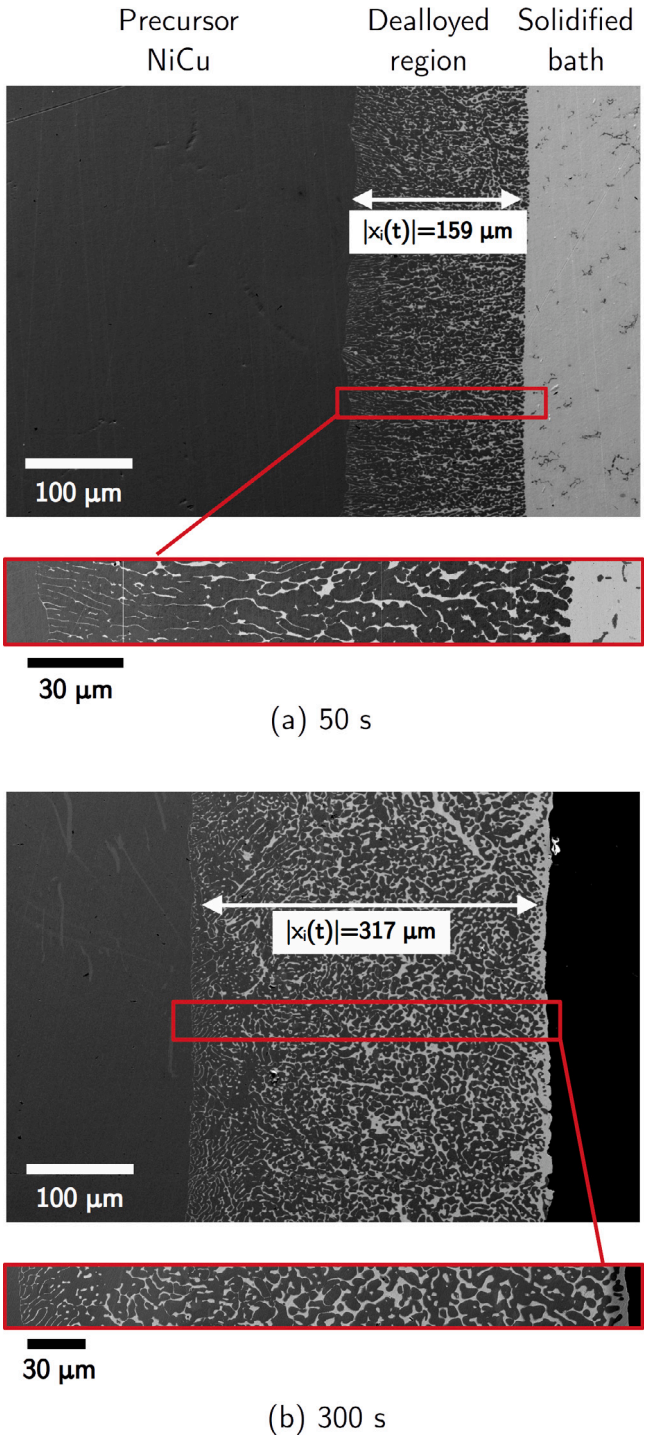

Fig. 3. SEM-BSE micrographs of dealloyed $Ni_{50}Cu_{50}$ samples at 1000 °C for immersion times (a) 50 s and (b) 300 s.

Fig. 3 shows examples of SEM-BSE (SEM, Ultra55, Zeiss, Germany) cross-sections of microstructures obtained by immersing $Ni_{50}Cu_{50}$ precursor in pure Ag liquid for 50 s and 300 s. The dealloying front (i.e. the reaction layer) and the dealloying back (i.e. the initial position of the precursor/liquid interface) are easily identified on these cross-sections and the dealloyed depth $|x_i(t)|$ can be simply measured. These

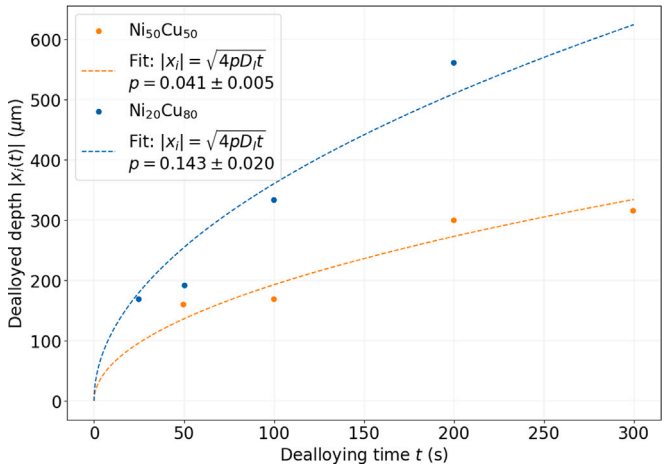

Fig. 4. Dealloyed depth as a function of immersion time for $Ni_{50}Cu_{50}$ and $Ni_{20}Cu_{80}$. Experimental (dots) and fitted data (dashed lines) for dealloying at 1000 °C.

measurements have been carried out for different dealloying times and results are reported on Fig. 4 that displays the dealloying depth as a function of the immersion time obtained for two precursors. Despite the experimental uncertainties, it is clear that the dealloying rate slows down in time for both precursors; this feature is ubiquitous in LMD experiments [13,24,33–35] and emerges from the fact that the dealloying process is limited by the diffusion of the sacrificial element in the liquid bath. As a diffusion-limited process, its kinetics can be modelled with a parabolic law: $|x_i(t)| = \sqrt{4pD_l t}$, where p is a dimensionless quantity referred to as the Péclet number [36]. Parabolic fits are reproduced with dash lines on Fig. 4 and the associated Péclet numbers are $p = 0.041 \pm 0.005$ and $p = 0.143 \pm 0.020$ for $Ni_{50}Cu_{50}$ and $Ni_{20}Cu_{80}$ precursors respectively.

The strong contrast between the ligaments (dark grey) and the liquid channels (light grey) visible in Fig. 3 allows to estimate the phase fractions of liquid and solid across the dealloyed layer. It appears that these phase fractions depend on the position in the dealloyed region: in particular, the fraction of liquid channels is smaller close to the dealloying front. The liquid fraction across the dealloyed layer is denoted $\rho(x)$ and its evolution will be discussed in the following sections.

The composition of the ligaments and the liquid was also determined using energy-dispersive X-ray spectroscopy (EDX). The cooling of the sample was fast enough (few seconds) to consider that the exchange between solid and liquid phases were limited and that the composition of the ligaments are representative of the high-temperature equilibrium. However, as the Ag–Cu phase diagram exhibits an eutectic transformation (see Fig. 1), the composition of solidified liquid displays inhomogeneities with Ag-rich and Cu-rich regions. To estimate the composition of the liquid phase, we first measured the total composition of Ag, Cu and Ni along a thin slice at a specific position x of the dealloyed region. The composition profile along this slice allowed to distinguish between zones corresponding to ligaments and those corresponding to the solidified bath. By averaging the compositions of each zone, we could estimate the compositions of the solidified bath and the ligaments. This measurement is therefore indirect and is very sensitive to the measure of the liquid fraction, increasing the uncertainty associated with this quantity.

4. Diffusion models for liquid metal dealloying

To simulate the kinetics of the dealloying process and the resulting morphologies, we propose diffusion models sharing similarities with the approaches of the literature [14,23]. In particular, we consider that the dealloying front remains planar (a valid assumption in view of Fig. 3) and that the dealloying front consists of a reaction layer where the formation of liquid channels and solid ligaments takes place. In Section 4.1, we employ simplifying assumptions in order to solve analytically the diffusion problem associated to LMD. Section 4.2 is dedicated to the development of a numerical model that relaxes these simplifying assumptions to allow a quantitative comparison with experimental results.

4.1. Analytical models and maximum velocity criterion

In this section, we consider the situation schematically represented in Fig. 5. The position of the dealloying front is denoted $x_i(t)$ and we fix $x_i(t = 0) = 0$ the interface position at $t = 0$. Following a convention inherited from solidification processes and used in previous works [35], we will consider that $x_i < 0$ during the dealloying process. In addition, the interface velocity (i.e. the dealloying rate) is defined as $v_i = \frac{\partial x_i}{\partial t}$.

The diffusion processes in the direction perpendicular to the dealloying reaction are considered to occur quickly because of the short lateral dimensions of the ligaments and liquid channels in this direction. Thus, the composition profiles that control the dealloying rate are one-dimensional. Second, we assume that the dealloying front is a transformation layer where the components of the precursor reorganizes into solid ligaments and Ag-rich liquid channels, with compositions that follow a thermodynamic equilibrium. The ternary phase diagram depicted in Fig. 2 shows that multiple equilibria are possible at the dealloying front, as a consequence of the Gibbs phase rule [36]. These multiple equilibria can be represented through an auxiliary variable θ that satisfies $0 < \theta < 1$ and that lists the tie-lines of increasing Cu composition: the tie-line $\theta = 0$ (respectively $\theta = 1$) corresponds to the Ni–Ag (resp. Ag–Cu) binary equilibrium. The equilibrium atomic compositions of the solid and liquid phases denoted $X^{(l)}_{Ni}(\theta)$, $X^{(l)}_{Cu}(\theta)$, $X^{(s)}_{Ni}(\theta)$ and $X^{(s)}_{Cu}(\theta)$ are then uniquely defined by the variable θ as shown on Fig. 6. We will assume that the dealloying front is characterized by an equilibrium θ_i that defines the compositions of the liquid channels and solid ligaments at the interface and that remains constant over time.

At the temperature of interest, the diffusion coefficient in the solid phases (ligaments and precursor) are several order of magnitude smaller than diffusion in the liquid. In addition, it was shown experimentally that the dealloying kinetics is controlled by diffusion of the sacrificial element in the liquid phase [10,13,23]. As a consequence, we neglect the influence of solid diffusion. To incorporate the fact that the diffusion only takes place in the liquid, we denote the volume fraction of the liquid by ρ and its value at the dealloying front by ρ_i.

As the dealloying reaction progresses, the amounts of Ni and Cu of the precursor alloy are distributed in the ligaments and the liquid channels. In addition, the diffusion in the liquid channels drains an amount of Ni and Cu away from the dealloying front. For simplicity reasons, we will consider in this section that the different species share the same atomic volume that does not depend on the phase (solid or liquid).

With all these considerations, mass conservation of Ni and Cu at the dealloying front can be written as:

$$v_i \left(X^{(p)}_{Ni} - \rho_i X^{(l)}_{Ni}(\theta_i) - (1-\rho_i) X^{(s)}_{Ni}(\theta_i) \right) = \rho_i D_l \left. \frac{\partial X^{(l)}_{Ni}}{\partial x} \right|_i = \rho_i J_{Ni} \quad (1)$$

$$v_i \left(X^{(p)}_{Cu} - \rho_i X^{(l)}_{Cu}(\theta_i) - (1-\rho_i) X^{(s)}_{Cu}(\theta_i) \right) = \rho_i D_l \left. \frac{\partial X^{(l)}_{Cu}}{\partial x} \right|_i = \rho_i J_{Cu} \quad (2)$$

Eqs. (1) and (2) relate the dealloying rate v_i to the tie-line θ_i and the flux of solutes J_{Cu} and J_{Ni}.

To keep the calculations tractable analytically, we consider in this section that the volume fraction of liquid channels remains constant in the dealloyed layer, i.e. $\forall x$, $\rho(x) = \rho_i$. This assumption is later relaxed in the numerical model developed in Section 4.2. As a consequence, the

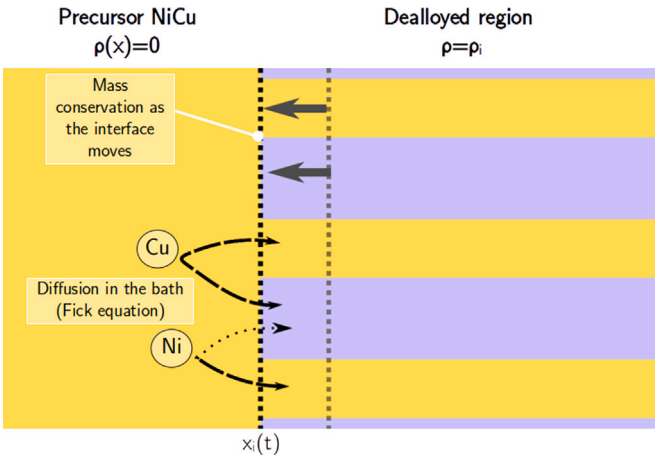

Fig. 5. Principle of the model for analytical resolution.

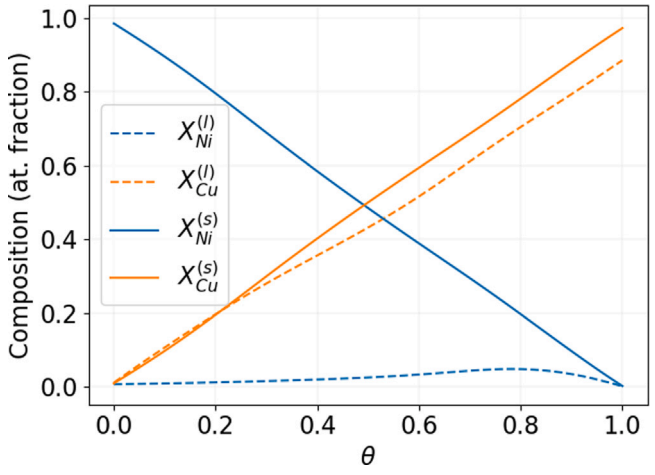

Fig. 6. Equilibrium compositions $X^{(l)}_{\mathrm{Ni}}(\theta)$, $X^{(l)}_{\mathrm{Cu}}(\theta)$, $X^{(s)}_{\mathrm{Ni}}(\theta)$ and $X^{(s)}_{\mathrm{Cu}}(\theta)$ as functions of the tie-line θ.

diffusion of Cu and Ni in the liquid channels are assumed to follow the Fick diffusion equation:

$$\frac{\partial X^{(l)}_n}{\partial t} = D_l \frac{\partial^2 X^{(l)}_n}{\partial x^2}, \qquad n = \mathrm{Cu, Ni}. \tag{3}$$

4.1.1. Linear profiles approximation

As a first approach, we consider that the diffusion profiles are subjected to fixed boundary conditions at $x = 0$, i.e. at the dealloying back. This type of boundary condition can be justified by considering that convection fluxes, originating from composition-dependent density of the liquid, mix continuously Cu in the large Ag bath [13,23], such that the composition at the dealloying back remains pure Ag. With such boundary conditions, the composition profiles between the dealloying front ($X^{(l)}_{\mathrm{Ni}}(\theta_i)$ and $X^{(l)}_{\mathrm{Cu}}(\theta_i)$) and the dealloying back can be assumed to be linear to the first order.

As a consequence, the fluxes of Ni and Cu can be written as:

$$J_{\mathrm{Ni}} = D_l \frac{X^{(l)}_{\mathrm{Ni}}(\theta_i)}{x_i} \tag{4}$$

$$J_{\mathrm{Cu}} = D_l \frac{X^{(l)}_{\mathrm{Cu}}(\theta_i)}{x_i} \tag{5}$$

Equating the velocities in Eqs. (1) and (2) yields an expression of ρ_i. Using Eqs. (4) and (5) for the fluxes, we obtain that ρ_i can be defined as a function of θ_i alone:

$$\rho_i(\theta_i) = \frac{X^{(l)}_{\mathrm{Ni}}(\theta_i)\left[X^{(p)}_{\mathrm{Cu}} - X^{(s)}_{\mathrm{Cu}}(\theta_i)\right] - X^{(l)}_{\mathrm{Cu}}(\theta_i)\left[X^{(p)}_{\mathrm{Ni}} - X^{(s)}_{\mathrm{Ni}}(\theta_i)\right]}{X^{(l)}_{\mathrm{Ni}}(\theta_i)\left[X^{(l)}_{\mathrm{Cu}}(\theta_i) - X^{(s)}_{\mathrm{Cu}}(\theta_i)\right] - X^{(l)}_{\mathrm{Cu}}(\theta_i)\left[X^{(l)}_{\mathrm{Ni}}(\theta_i) - X^{(s)}_{\mathrm{Ni}}(\theta_i)\right]} \tag{6}$$

At this point, it is convenient to introduce the dimensionless Péclet number $p = \frac{x_i v_i}{2D_l}$ frequently used in diffusion-related problems [36]. Combining Eqs. (2) and (5), we get:

$$p(\theta_i) = \frac{\rho_i(\theta_i)\, X^{(l)}_{\mathrm{Cu}}(\theta_i)}{2\left(X^{(p)}_{\mathrm{Cu}} - \rho(\theta_i) X^{(l)}_{\mathrm{Cu}}(\theta_i) - (1-\rho(\theta_i)) X^{(s)}_{\mathrm{Cu}}(\theta_i)\right)} \tag{7}$$

Because the boundary conditions at the dealloying front and at the dealloying back are assumed to remain unchanged over time, p is constant and the diffusion problem is self-similar [36]. With p constant, the differential equation $x_i v_i = 2pD_l$ admits a single solution of the form:

$$x_i(\theta_i, t) = -\sqrt{4p(\theta_i) D_l t} \tag{8}$$

We note that the dealloying rate as well as the properties of the dealloying front (compositions and phase fractions) are functions of the tie-line θ_i that describes the equilibrium of the interface.

Eq. (8) can be seen as an upper-bound for the dealloying kinetics. Indeed, assuming that convection currents maintain a pure Ag liquid at the dealloying back is certainly ideal and overestimates the fluxes of species away from the dealloying front, thereby overestimating the dealloying rate.

4.1.2. Time-dependent profiles

An alternative is to integrate time-dependent diffusion equations in an infinite medium. In this case, it is assumed that the ligament structure extend beyond the dealloying back with the same volume fraction $\rho = \rho_i$ of liquid channels. The resulting kinetics can be considered as a lower-bound limit for the dealloying rate because it overestimates the influence of the ligament structure inhibiting the diffusion of the sacrificial element.

Lai et al. [14] showed that in the case of a diffusion occurring in pure liquid without ligaments ($\rho = 1$), the self-similar solution fixes unique values of the interfacial concentrations $X^{(l)}_{\mathrm{Ni}}(\theta_i)$ and $X^{(l)}_{\mathrm{Cu}}(\theta_i)$. In other words, the tie-line θ_i at the interface is uniquely determined by the integration of the diffusion equation in the liquid. In this study, we tackle the case where both ligaments and liquid channels are formed at the dealloying front. In such case, the equilibrium is not uniquely determined.

To solve Eqs. (1)–(3) with these assumptions, we follow Ref. [14] and introduce the variable $z(x,t) = x/x_i(t)$ ($z = 0$ at the dealloying back and $z = 1$ at the dealloying front) and derive the following relations for the composition fields $X^{(l)}_n$ in the liquid:

$$\frac{\partial X^{(l)}_n}{\partial t} = -\frac{z v_i}{x_i}\frac{\partial X^{(l)}_n}{\partial z}$$

$$\frac{\partial X^{(l)}_n}{\partial x} = \frac{1}{x_i}\frac{\partial X^{(l)}_n}{\partial z}, \qquad n = \mathrm{Cu, Ni}$$

$$\frac{\partial^2 X^{(l)}_n}{\partial x^2} = \frac{1}{x_i^2}\frac{\partial^2 X^{(l)}_n}{\partial z^2}$$

Using these relations, Eq. (3) can be written as partial differential equations on z:

$$2pz\frac{\partial X^{(l)}_n}{\partial z} + \frac{\partial^2 X^{(l)}_n}{\partial z^2} = 0, \qquad n = \mathrm{Cu, Ni}. \tag{9}$$

Eqs. (1)–(2) provide the following boundary conditions:

$$\left.\frac{\partial X^{(l)}_{\mathrm{Ni}}}{\partial z}\right|_{z=1} = 2pA(\theta_i, \rho_i)$$

$$\text{with} \quad A(\theta_i, \rho_i) = \frac{X^{(p)}_{\mathrm{Ni}} - \rho X^{(l)}_{\mathrm{Ni}}(\theta_i) - (1-\rho_i) X^{(s)}_{\mathrm{Ni}}(\theta_i)}{\rho_i} \tag{10}$$

$$\left.\frac{\partial X_{\mathrm{Cu}}^{(l)}}{\partial z}\right|_{z=1} = 2pB(\theta_i,\rho_i) \quad \text{with} \quad B(\theta_i,\rho_i) = \frac{X_{\mathrm{Cu}}^{(p)} - \rho X_{\mathrm{Cu}}^{(l)}(\theta_i) - (1-\rho_i)X_{\mathrm{Cu}}^{(s)}(\theta_i)}{\rho_i} \tag{11}$$

Integrating Eq. (9) and using these boundary conditions yields:

$$\frac{\partial X_{\mathrm{Ni}}^{(l)}}{\partial z} = 2pA(\theta_i,\rho_i)e^{p(1-z^2)} \tag{12}$$

$$\frac{\partial X_{\mathrm{Cu}}^{(l)}}{\partial z} = 2pB(\theta_i,\rho_i)e^{p(1-z^2)} \tag{13}$$

These relations can be further integrated to obtain the composition profiles. Assuming a pure Ag bath far away from the precursor we have $X_{\mathrm{Ni}}(z=-\infty) = X_{\mathrm{Cu}}(z=-\infty) = 0$, resulting in the following relations for the composition profiles:

$$X_{\mathrm{Ni}}^{(l)}(z) = A(\theta_i,\rho_i)e^p\sqrt{\pi p}\left(\mathrm{erf}(\sqrt{pz})+1\right) \tag{14}$$

$$X_{\mathrm{Cu}}^{(l)}(z) = B(\theta_i,\rho_i)e^p\sqrt{\pi p}\left(\mathrm{erf}(\sqrt{pz})+1\right) \tag{15}$$

Finally, the boundary condition at the dealloying front ($z=1$): $X_{\mathrm{Ni}}(z=1) = X_{\mathrm{Ni}}^{(l)}(\theta_i)$ and $X_{\mathrm{Cu}}(z=1) = X_{\mathrm{Cu}}^{(l)}(\theta_i)$ gives the following equations that relate three unknowns of the problem p, θ_i and ρ_i:

$$X_{\mathrm{Ni}}^{(l)}(\theta_i) = A(\theta_i,\rho)e^p\sqrt{\pi p}\left(\mathrm{erf}(\sqrt{p})+1\right) \tag{16}$$

$$X_{\mathrm{Cu}}^{(l)}(\theta_i) = B(\theta_i,\rho)e^p\sqrt{\pi p}\left(\mathrm{erf}(\sqrt{p})+1\right) \tag{17}$$

As in Section 4.1.1, the problem is not fully determined as we have more unknowns than equations. It is however possible to fix θ_i and to use Eqs. (16)–(17) to obtain ρ_i and p. In particular, p can be removed from Eqs. (16)–(17) by computing the ratio $X_{\mathrm{Ni}}^{(l)}(\theta_i)/X_{\mathrm{Cu}}^{(l)}(\theta_i)$, yielding an expression of ρ_i. We recover thereby Eq. (6), showing the equivalence between both analytical treatments. Still considering a given value of θ_i, Eq. (16) (or equivalently Eq. (17)) is solved numerically to determine p. As in Section 4.1.1, a constant value of p yields the time-evolution of the position of the dealloying front given by Eq. (8).

4.1.3. Comparison between analytical models — extremum criterion

Both analytical solutions presented in Sections 4.1.1 and 4.1.2 yield relations between the interface tie-line θ_i (that characterizes the equilibrium at the dealloying front) and the Péclet number p of the dealloying process. These relations are shown in the upper panels of Fig. 7 for two compositions of the precursor alloy.

We note that not all values of θ_i lead to valid solutions of the diffusion problem. In particular, above a critical value θ_{max} that depends on the precursor content, Eq. (6) yields a negative value of the liquid fraction ρ_i, which is nonphysical. Interestingly, for both approaches, the Péclet number depends non-monotonously on θ_i in the range $0 < \theta_i < \theta_{max}$: small values of θ_i represent the formation of Ni-rich ligaments in equilibrium with liquid channels retaining a small amount of Cu (see Figs. 2 and 6). The resulting gradient of Cu in the liquid channels is then very small, which limits the diffusion of Cu away from the dealloying front and thus the dealloying kinetics. Larger values of θ_i allows for steeper gradients of Cu in the liquid, thereby promoting the dealloying reaction. But for values of θ_i approaching θ_{max}, ρ decreases towards 0, which again limits the diffusion of solutes away from the interface and reduces the dealloying kinetics. In between, p (and the dealloying rate) is maximum for intermediate values of θ_i that lead to the formation of liquid channels and solid ligaments containing significant amounts of the sacrificial element Cu.

Different values of θ_i also correspond to specific interfacial compositions and liquid fractions that are shown in the lower panel of Fig. 7, allowing for a comparison with experimental measurements. Indeed, the values ρ_i, $X_{\mathrm{Cu}}^{(s)}(\theta_i)$ and $X_{\mathrm{Cu}}^{(l)}(\theta_i)$ can be determined close to the interface by SEM and EDS techniques (see Section 3) and the measured values are reported on the lower panels of Fig. 7. The experimental measurements bear some uncertainty that are represented with error bars.

Fig. 7 shows that for both precursor compositions, experimental measurements of the liquid fraction and ligament composition correspond to a similar value of θ_i. This equilibrium coincides with the tie-line maximizing the Péclet number which is indicated with dashed lines on Fig. 7. Maximizing the Péclet number is equivalent to maximizing the velocity of the dealloying front, and we will consider in the following that the interface tie-line θ_i is selected by such maximum velocity criterion.

We note that the liquid compositions at the interface do not quite match this equilibrium, which can be attributed to the large uncertainties associated with this indirect measurement (see Section 3). Despite this discrepancy, the evolution of the interface compositions in both phases with the precursor content is consistent with the maximum velocity criterion: when the precursor is richer in Cu, experiments showed that the interface compositions of Cu increase in both phases. This trend is well reproduced by the maximum velocity criterion that predicts an equilibrium at higher θ_i.

The analytical solutions proposed in this section rely on multiple assumptions that can be refined: first, the interface equilibrium θ_i is considered to be constant in time. However, phase field simulations revealed that the interfacial equilibrium tended to change as the dealloying reaction progresses [14]. Moreover, both analytical approaches assume that the fraction of liquid channels does not change in the dealloying region while microstructures displayed on Fig. 3 show that liquid channels appear wider away from the dealloying front. To keep derivation simple, we also neglected the difference of molar volume between different species, which may affect the results. These assumptions are relaxed in the numerical diffusion model presented in the following section.

4.2. Numerical diffusion model

To relax the simplifying assumptions necessary to derive the analytical approaches, we propose in this section a numerical diffusion model providing a less idealized description of the dealloying process.

First, we take into account the different molar volumes of the species, assuming that they do not depend on the phase they belong to. The volume fractions are denoted $c_n^{(\phi)}$, with:

$$c_n^{(\phi)} = \frac{X_n^{(\phi)}V_n^m}{X_{\mathrm{Ni}}^{(\phi)}V_{\mathrm{Ni}}^m + X_{\mathrm{Cu}}^{(\phi)}V_{\mathrm{Cu}}^m + X_{\mathrm{Ag}}^{(\phi)}V_{\mathrm{Ag}}^m} \quad n=\mathrm{Cu,Ni,Ag}; \quad \phi = l,s \tag{18}$$

We take $V_{\mathrm{Ni}}^m = 6.59\ \mathrm{cm^3/mol}$, $V_{\mathrm{Cu}}^m = 7.11\ \mathrm{cm^3/mol}$, and $V_{\mathrm{Ag}}^m = 10.27\ \mathrm{cm^3/mol}$ [37]. Taking into account the molar volumes of different species, Eqs. (1) and (2) become:

$$v_i\left(c_{\mathrm{Ni}}^{(p)} - \rho_i c_{\mathrm{Ni}}^{(l)}(\theta_i) - (1-\rho_i)c_{\mathrm{Ni}}^{(s)}(\theta_i)\right) = \rho_i D_l \left.\frac{\partial c_{\mathrm{Ni}}^{(l)}}{\partial x}\right|_i = \rho_i J_{\mathrm{Ni}}, \tag{19}$$

$$v_i\left(c_{\mathrm{Cu}}^{(p)} - \rho_i c_{\mathrm{Cu}}^{(l)}(\theta_i) - (1-\rho_i)c_{\mathrm{Cu}}^{(s)}(\theta_i)\right) = \rho_i D_l \left.\frac{\partial c_{\mathrm{Cu}}^{(l)}}{\partial x}\right|_i = \rho_i J_{\mathrm{Cu}}. \tag{20}$$

SEM observations displayed in Fig. 3 show that the ratio between solid ligaments and liquid channels varies in the dealloyed layer. This is attributed to the exchanges of species between both phases. Ligaments and liquid channels are assumed thin enough so that diffusion between them occurs quickly compared to the progression of the dealloying front. Hence, at a given position x in the dealloyed region, the liquid channels and the solid ligaments are assumed to reach quickly a thermodynamic equilibrium. The compositions $c_{\mathrm{Ni}}^{(l)}(x)$, $c_{\mathrm{Cu}}^{(l)}(x)$, $c_{\mathrm{Ni}}^{(s)}(x)$ and $c_{\mathrm{Cu}}^{(s)}(x)$ and the liquid fraction $\rho(x)$ are determined by this equilibrium. At a given position x in the dealloyed region, this change of composition occurs continuously along the dealloying process: indeed, because of the movement of the dealloying front, the gradient of Cu in the dealloyed region becomes less and less steep, so that the composition of Cu in the liquid at x decreases continuously in time. This change

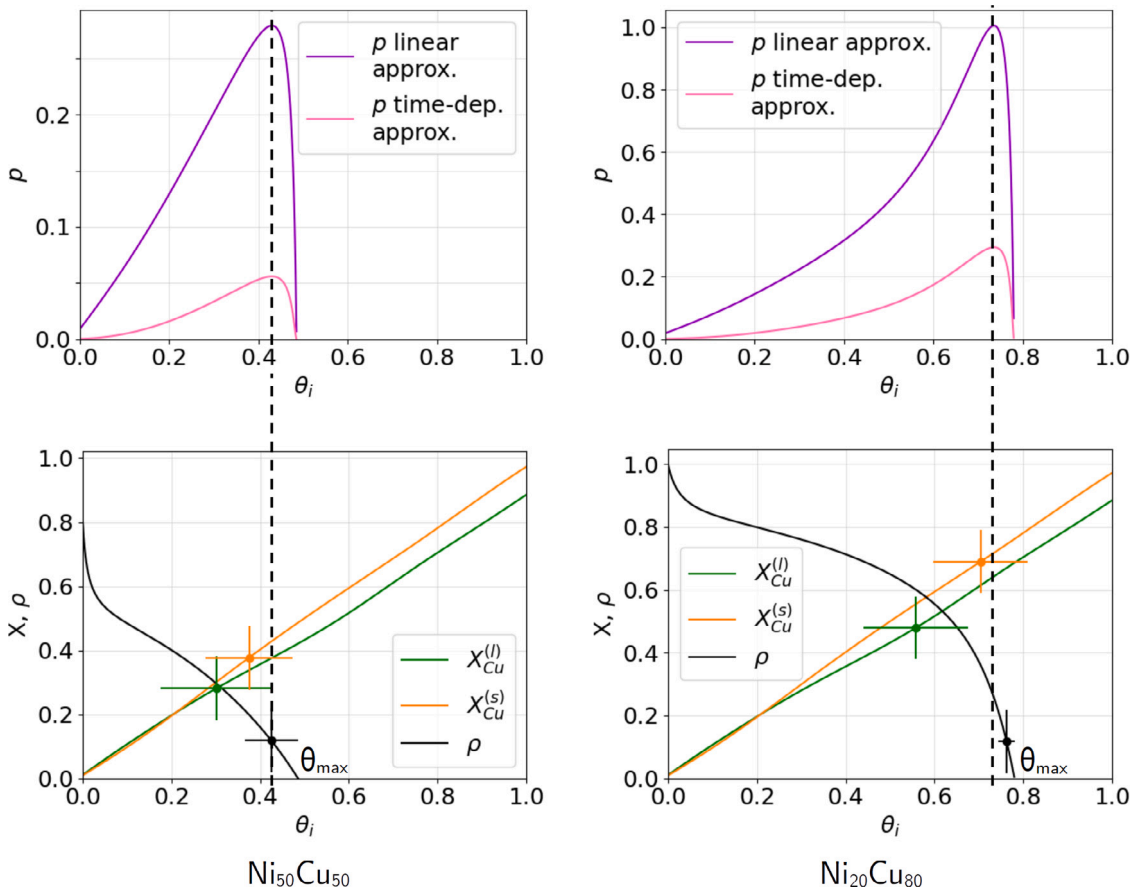

Fig. 7. Péclet number p and interfacial quantities $X^{(l)}_{Cu}$, $X^{(s)}_{Cu}$ and ρ as functions of θ for $Ni_{50}Cu_{50}$ and $Ni_{20}Cu_{80}$ precursors, analytical results (solid lines) and experimental data (dots). The vertical black dotted lines indicate for both precursor compositions the value of θ corresponding to a maximum value of p.

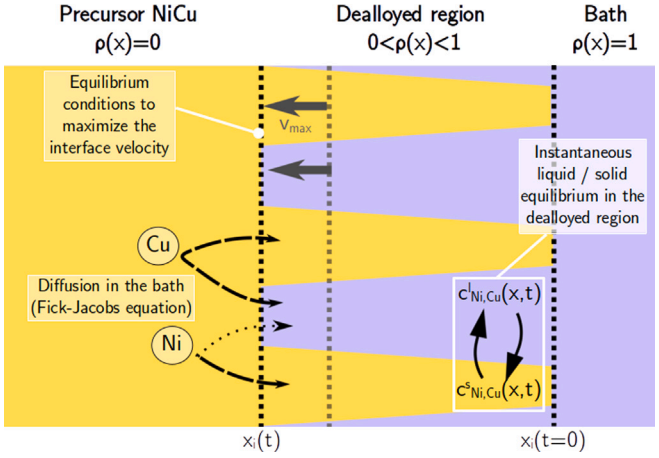

Fig. 8. Principle of the numerical model.

of composition of the liquid is then accompanied by the change of composition of the solid and the change of liquid fraction $\rho(x)$.

Because of this thermodynamic equilibrium between liquid channels and solid ligaments, the fraction of liquid channels $\rho(x,t)$ varies both with position x and time t (see Fig. 8), and diffusion occurs in channels of varying cross-sections. A way to incorporate this effect may be to integrate Fick's equation in 3D around conical ligaments to account for the role of solute fluxes non-parallel to the dealloying direction. However, if the cross-section varies smoothly in the structure, it was shown theoretically and numerically [38] that the diffusion of the species obeys the following diffusion equation modified to incorporate the role of the varying liquid fraction:

$$\frac{\partial c_n(x,t)}{\partial t} = D_l \frac{\partial}{\partial x}\left[\rho(x)\frac{\partial}{\partial x}\left(\frac{c_n(x,t)}{\rho(x)}\right)\right], \qquad n = \mathrm{Cu}, \mathrm{Ni} \tag{21}$$

This relation is referred to as the Fick–Jacobs diffusion equation [38, 39] and is used to describe the diffusion of both Ni and Cu in the liquid bath. Beyond the dealloying back (i.e. for $x > 0$), $\rho(x) = 1$ and we consider that the diffusion takes place in a pure liquid bath. The size of the liquid bath is chosen large enough such that it does not influence the dealloying process, thereby mimicking an infinite bath.

We consider that the equilibrium at the interface varies with time and is characterized by the variable $\theta_i(t)$. A given value of θ_i dictates the interface concentrations of each species, that in turn dictate the flux of the species in the liquid and the fraction of the liquid channels ρ_i at the interface obtained by combining Eqs. (1) and (2):

$$\rho_i(\theta_i) = \frac{J_{\mathrm{Ni}}\left[X^{(p)}_{\mathrm{Cu}} - X^{(s)}_{\mathrm{Cu}}(\theta_i)\right] - J_{\mathrm{Cu}}\left[X^{(p)}_{\mathrm{Ni}} - X^{(s)}_{\mathrm{Ni}}(\theta_i)\right]}{J_{\mathrm{Ni}}\left[X^{(l)}_{\mathrm{Cu}}(\theta_i) - X^{(s)}_{\mathrm{Cu}}(\theta_i)\right] - J_{\mathrm{Cu}}\left[X^{(l)}_{\mathrm{Ni}}(\theta_i) - X^{(s)}_{\mathrm{Ni}}(\theta_i)\right]} \tag{22}$$

As in Section 4.1.2, the choice of the interface equilibrium θ_i is not unique and leads to different interface compositions, liquid fractions and interface velocities. Some values of θ_i can be discarded because they lead to unphysical values of the liquid fraction $\rho_i < 0$ or $\rho_i > 1$. Following the maximum criterion introduced in Section 4.1.2, we choose θ_i to maximize the interface velocity along the simulation.

To implement numerically the model, we discretize space and time with steps Δx and Δt. The numerical integration of the model consists in iterations of the following steps:

1. Considering the composition and the liquid fraction fields at time t, the interface tie-line θ_i is chosen to maximize the dealloying rate v_i.
2. The Fick–Jacobs equations for Ni and Cu are integrated numerically in the dealloyed and liquid regions with an Euler explicit scheme:

$$c_{j,t+\Delta t} = c_{j,t} + \frac{D_l \Delta t}{\Delta x}\left(\frac{J_{j+1/2} - J_{j-1/2}}{\Delta x}\right) \tag{23}$$

$$= c_{j,t} + \frac{D_l \Delta t}{\Delta x^2}\left(\frac{\rho_{j+1,t} + \rho_{j,t}}{2}\left(\frac{c_{j+1,t}}{\rho_{j+1,t}} - \frac{c_{j,t}}{\rho_{j,t}}\right) - \frac{\rho_{j,t} + \rho_{j-1,t}}{2}\left(\frac{c_{j,t}}{\rho_{j,t}} - \frac{c_{j-1,t}}{\rho_{j-1,t}}\right)\right). \tag{24}$$

   The fluxes are computed between grid points where the value of ρ is linearly interpolated.
3. The position of the interface is integrated with time:

$$x_i(t + \Delta t) = x_i(t) + \Delta t v_i \tag{25}$$

4. At each location of the dealloyed region, the composition of both liquid channels and ligaments as well as the liquid fraction are updated to satisfy a thermodynamic equilibrium. This is performed with the Python plug-in of the software Thermo-Calc [40]. To avoid numerical instabilities, this update is not performed on the two grid points immediately next to the interface location; the size of this buffer region does not influence the results discussed below.

The numerical integration is performed with $\Delta x = 10\,\mu m$ and $\Delta t = 10^{-3}$ s. The model provides the dealloying depth as a function of time as well as the composition profiles in the dealloyed region. Both of these results are discussed in the following section.

5. Results and comparison with experimental measurements

5.1. Dealloying kinetics

The dealloying kinetics for a $Ni_{50}Cu_{50}$ precursor in a pure Ag bath obtained from both analytical and numerical models are compared on Fig. 9.a. Both analytical models frame the results obtained from the integration of the numerical approach: as expected from the assumptions of analytical models, the linear profile approximation significantly overestimates the diffusive fluxes and then the dealloying kinetics. Conversely, the time-dependent analytical solution underestimates the dealloying kinetics obtained numerically because of the influence of infinitely long ligaments. The dealloying kinetics obtained from the numerical model can be fitted with $|x_i(t)| = \sqrt{4pD_l t}$ (dashed blue line on Fig. 9.a), yielding an estimate of the corresponding Péclet number. The fit reproduces faithfully the dealloying kinetics obtained numerically but a slight shift between the data and the fit is clearly visible. This can be attributed to (i) the variable interface composition, potentially yielding a slowly varying Péclet number, (ii) the fact that the liquid fraction in the dealloyed region $\rho(x)$ is constantly adjusted in the numerical model, influencing the integration of the diffusion equation over time. Consequently, the numerical simulations slightly differ from a scenario solely governed by a unique Péclet number.

Fig. 9.b generalizes the previous observations to various precursor compositions by displaying the product pD_l as a function of the precursor composition $X^{(p)}_{Ni}$. Similarly to Fig. 9.a, the dealloying kinetics obtained numerically are fitted with $|x_i(t)| = \sqrt{4pD_l t}$ to obtain a value of the Péclet number p. As in the case of Fig. 9.a, both analytical models frame the results obtained with the numerical approach. The different approaches demonstrate that the dealloying rate decreases with increasing content of Ni in the precursor: more Ni in the precursor leads to a larger solid fraction in the dealloyed region, and a smaller liquid fraction where diffusion takes place, thereby reducing the dealloying rate.

The product pD_l deduced from experimental results (Fig. 4) is also reported in Fig. 9.b (red data points), showing that the analytical and numerical models overestimate significantly the experimental kinetics.

This discrepancy can be attributed to the simplifying assumptions of the model. Firstly, the diffusion coefficient used here has been assessed for dilute solutions of Cu in Ag while the concentration of Cu in the bath reaches values as high as 70 at.%, which certainly modifies the value of the diffusion coefficient. Secondly, the equilibrium between solid ligaments and liquid channels in the dealloyed region is assumed to occur instantaneously, and the influence of the transient regime associated to these diffusion processes is neglected. Thirdly, the diffusion is considered to take place in straight channels, while liquid channels in dealloyed structures are tortuous (see Fig. 3 and Refs. [41,42]). This tortuosity denoted τ extends the length of the diffusion path and is defined as the ratio between the shortest path through liquid channels between two points and the straight line linking these points ($\tau > 1$). Incorporating the effect of tortuosity can be done by rescaling the diffusion coefficient as $D'_l = D_l/\tau^2$ [43].

These reasons can be invoked to explain the discrepancy between numerical and experimental kinetics. As shown in Fig. 9.b, applying a correction to the diffusion coefficient such that $D'_l = D_l/2.6$ (that may be attributed to the deviation from the dilute limit or to the role the tortuosity) allows our numerical prediction to fall very close to experimental measurements.

5.2. Equilibrium at the dealloying front

In the work by Lai et al. [14], phase field simulations showed that the composition of the sacrificial element in the liquid channels at the dealloying front varies in time and seems to increase logarithmically with the dealloying depth. This phenomenological logarithmic evolution was suggested to connect phase field results with experimental measurements performed on the TaTiCu system.

As in phase field modelling, the numerical approach described in Section 4.2 also captures the time-evolution of the composition at the dealloying front. To clarify the origin of this evolution, we use a simplified version of the numerical model where the equilibria in the dealloyed region are not updated after the formation of the ligaments, and where the molar volumes are assumed to be equal. Beforehand, it was verified that these simplifications did not influence the results of the model discussed here.

Fig. 10 displays the evolution of the interface composition $X^{(l)}_{Cu}(\theta_i)$ as a function of the dealloying depth for two different precursor compositions. For both precursor compositions, the interface composition $X^{(l)}_{Cu}(\theta_i)$ increases as the dealloying reaction progresses, in agreement with the results of Lai et al. [14]. We highlight here that the evolution of $X^{(l)}_{Cu}(\theta_i)$ in the numerical model is a direct consequence of the maximum velocity criterion.

In order to clarify this evolution, we suggest to explain it as a consequence of this criterion. By rewriting Eq. (2), we get:

$$v_i = \left(\frac{\rho_i}{X^{(p)}_{Cu} - \rho_i X^{(l)}_{Cu}(\theta_i) - (1-\rho_i) X^{(s)}_{Cu}(\theta_i)}\right) J_{Cu} \tag{26}$$

where J_{Cu} is the flux of Cu in the dealloyed region. This quantity can be expressed as $(X^{(l)}_{Cu}(\theta_i) - X^{(l)}_{Cu,d})/d$ where $X^{(l)}_{Cu,d}$ denotes the composition at an arbitrary distance d small compared to the diffusion length.

Using a similar expression for the flux of Ni in the liquid channels, Eq. (22) can be written as:

$$\rho_i = \frac{\left(X^{(l)}_{Ni}(\theta_i) - X^{(l)}_{Ni,d}\right)\left[X^{(p)}_{Cu} - X^{(s)}_{Cu}(\theta_i)\right] - \left(X^{(l)}_{Cu}(\theta_i) - X^{(l)}_{Cu,d}\right)\left[X^{(p)}_{Ni} - X^{(s)}_{Ni}(\theta_i)\right]}{\left(X^{(l)}_{Ni}(\theta_i) - X^{(l)}_{Ni,d}\right)\left[X^{(l)}_{Cu}(\theta_i) - X^{(s)}_{Cu}(\theta_i)\right] - \left(X^{(l)}_{Cu}(\theta_i) - X^{(l)}_{Cu,d}\right)\left[X^{(l)}_{Ni}(\theta_i) - X^{(s)}_{Ni}(\theta_i)\right]} \tag{27}$$

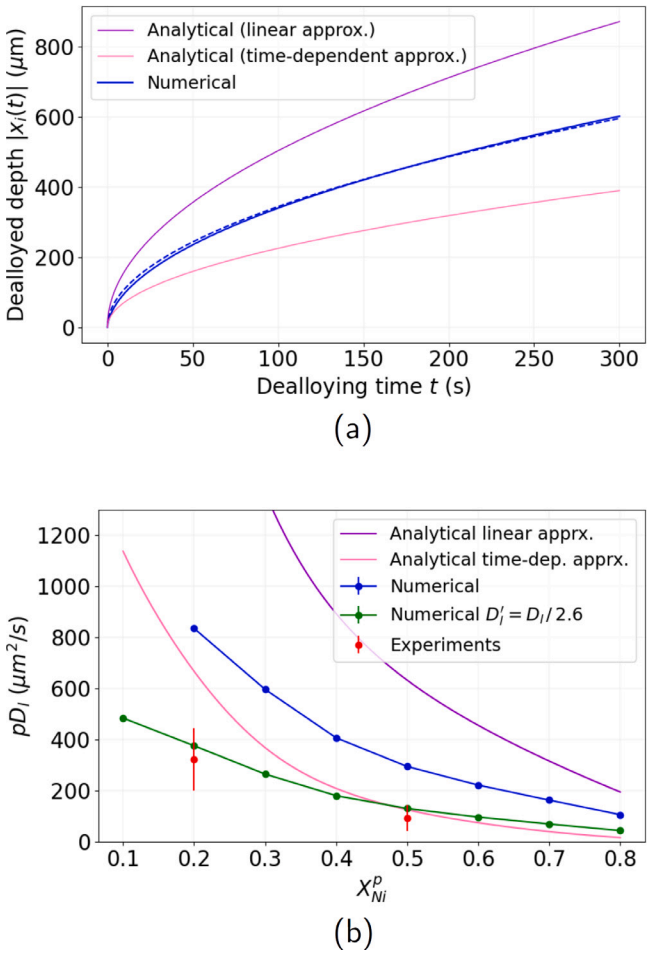

Fig. 9. Simulated and measured kinetics. (a) Dealloyed depth vs. dealloying times for a $Ni_{50}Cu_{50}$ precursor. Numerical prediction was fitted assuming a parabolic law ($|x_i(t)| = \sqrt{4pD_i t}$). (b) Product pD_l as a function of the precursor composition in Ni, comparison between numerical and experimental results. Error bars resulting from the fit of the numerical results are smaller than the size or the markers. (For interpretation of the references to colour in this figure legend, the reader is referred to the web version of this article.)

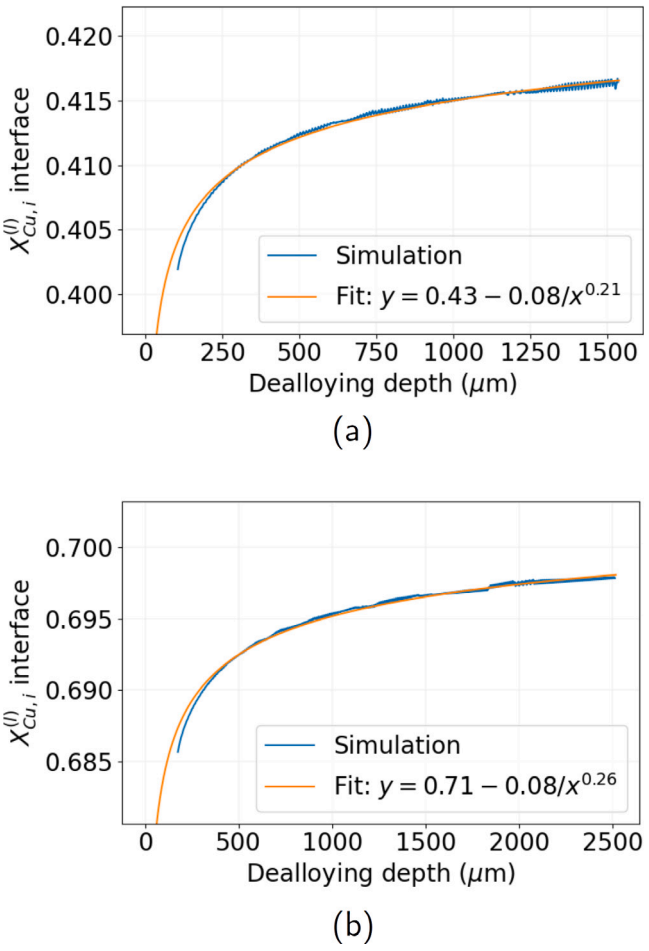

Fig. 10. Interface composition $X^{(l)}_{Cu}(\theta_i)$ as a function of the dealloyed depth. The simulated curves were convoluted with a running average to smooth down oscillations attributed to the movement of the interface from one grid point to the next. (a) Precursor $Ni_{50}Cu_{50}$. (b) Precursor $Ni_{20}Cu_{80}$.

As a first order approximation, the compositions $X^{(l)}_{Ni,d}$ and $X^{(s)}_{Cu,d}$ are considered to follow an equilibrium condition (i.e. to follow a tie-line). By fixing $X^{(l)}_{Cu,d}$, the interface equilibrium θ_i maximizing v_i (Eq. (26)) can be determined numerically, thereby fixing $X^{(l)}_{Cu}(\theta_i)$. Fig. 11 shows for a precursor $Ni_{50}Cu_{50}$ the evolution of the interface composition $X^{(l)}_{Cu}(\theta_i)$ and of the liquid fraction at the interface ρ_i as a function of the composition $X^{(l)}_{Cu,d}$. At the beginning of the dealloying reaction, the gradient of Cu in the liquid near the interface is high, which corresponds to low values of $X^{(l)}_{Cu,d}$. As the dealloying reaction progresses, the composition gradient stretches and becomes less sharp such that $X^{(l)}_{Cu,d} \to X^{(l)}_{Cu}(\theta_i)$. Fig. 11 shows that, as a consequence, the interface composition $X^{(l)}_{Cu}(\theta_i)$ (chosen to fulfil the maximum velocity criterion) increases. Concurrently with the increase of $X^{(l)}_{Cu}(\theta_i)$, the volume fraction of liquid at the interface ρ_i decreases according to Eq. (27).

The evolution of the interface composition $X^{(l)}_{Cu}(\theta_i)$ is expected to depend on the phase diagram and how the equilibrium compositions depend on one another. Moreover, $X^{(l)}_{Cu}(\theta_i)$ should not diverge. For these reasons, we discard the logarithmic trend considered in Ref. [14] and fit the evolution of the interface composition with a power law of the form $X^{(l)}_{Cu}(\theta_i) = X^{(l)}_{Cu}(\hat{\theta}_i) - B/|x_i|^m$, which incorporates a maximum bound for the value of $X^{(l)}_{Cu}(\theta_i)$ for $\theta_i = \hat{\theta}_i$. A satisfying fit was obtained (see Fig. 10.a), yielding a maximum value of the interface composition $X^{(l)}_{Cu}(\hat{\theta}_i) = 0.43$ for the $Ni_{50}Cu_{50}$ case. A similar fit was performed for the $Ni_{20}Cu_{80}$ precursor (see Fig. 10.b), yielding a different exponent m. The shape of these non-linear curves (i.e. the exponent m) is not universal and depends on the features of phase diagram in the vicinity of $\hat{\theta}$, that are embedded in the functions $X^{(\phi)}_n(\theta)$ depicted in Fig. 6 and entering Eq. (27).

Interestingly, Fig. 11 also demonstrates that the value of $X^{(l)}_{Cu}(\theta_i)$ cannot exceed a specific value. Above this threshold, $\rho_i < 0$ and there is no physically admissible solution to Eqs. (26)–(27).

5.3. Composition profiles

The numerical model also yields composition profiles of both liquid channels and solid ligaments as well as the evolution of the liquid fraction ρ across the dealloyed region (in contrast to the previous section, the model used here incorporates the exchanges between ligaments and liquid channels in the dealloyed region). On Fig. 12, these numerical profiles are compared with experimental measurements performed with SEM and EDX (see Section 3 for details) for $Ni_{50}Cu_{50}$ and $Ni_{20}Cu_{80}$ precursors dealloyed for 100 s in Ag at 1000 °C.

While the compositions at the dealloying interface (and their slow evolution with time) are discussed in the previous section, the composition of both solid and liquid phases do not remain constant after their formation. Indeed, the liquid metal dealloying process is allowed by the

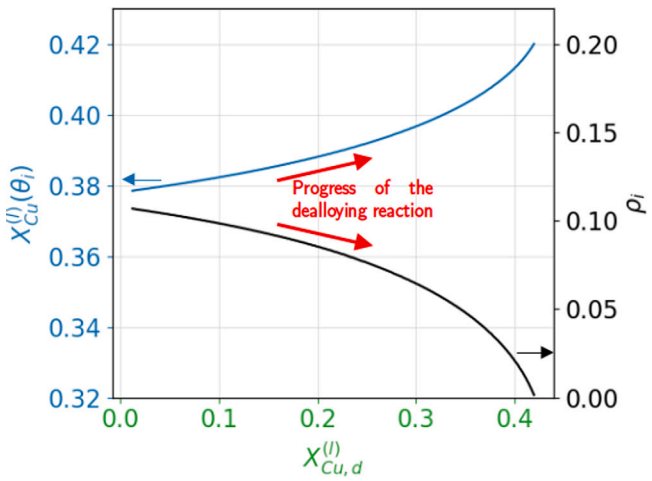

Fig. 11. $X^{(l)}_{\mathrm{Cu}}(\theta_i)$ and ρ_i as functions of the composition $X^{(l)}_{\mathrm{Cu},d}$ for the $Ni_{50}Cu_{50}$ precursor.

diffusion of sacrificial elements (here Cu) in the bath away from the dealloying front, that is related to the formation of Cu gradients in the liquid bath clearly visible on both numerical and experimental profiles (see Fig. 12.b and e). At a given position in the dealloying region, the composition of Cu in the bath decreases with time because of the continuous stretching of the Cu gradient with time. The surrounding solid ligaments then become out of equilibrium with the bath, which triggers the dissolution of Cu from the solid ligaments to the liquid bath. This is done instantaneously in the numerical model as the solid and liquid phase are updated to follow thermodynamic equilibria. The dissolution of Cu from the solid promotes the formation of a composition gradient in the solid clearly visible on Fig. 12.a and d. The exchanges between solid and liquid phases in the dealloyed region also promote the formation of a gradient of the liquid fraction in the dealloying region shown in Fig. 12.c and f: because of the release of Cu from the solid phase, the ligaments and the liquid channels become respectively thinner and wider away from the dealloying front. It is clear from Fig. 12 that the numerical model reproduces the expected gradients of compositions and microstructures obtained experimentally for both precursor contents.

In addition, it also reproduces the changes of composition obtained with different precursors: for the precursor $Ni_{20}Cu_{80}$ that contains more Cu than $Ni_{50}Cu_{50}$, both numerical and experimental results shows that the ligaments close to the dealloying front are richer in Cu. The same tendency is observed in the liquid even though the uncertainties of the experimental measurements make the trend less clear. Also, our predictions regarding the liquid fraction align with experimental observations: the dealloying of precursors with a higher Ni content leads to the formation of a larger fraction of ligaments (because of the low solubility of Ni in the bath) and thus a smaller fraction of liquid phase.

The agreement between numerical and experimental results demonstrates the capability of the numerical model to reproduce the microstructures obtained experimentally and their evolution with the precursor composition.

However, the composition profiles obtained numerically appear to be slightly shifted with respect to the experimental results; this can be seen clearly on the composition profiles for the solid. This mismatch is also visible for liquid compositions, however one should note that the indirect measurement of the liquid composition bears high uncertainties, translating into very scattered values. These discrepancies will be discussed in the last section.

6. Discussion

In this work, we have attempted to model liquid metal dealloying (LMD) as a 1D diffusion problem of solutes away from the dealloying front. Previously proposed diffusion models of the process considered the dissolution of the precursor in a pure liquid bath [14,23]. The associated diffusion problem is well defined and can be solved analytically from the diffusion of the solutes in a pure liquid phase. A limitation of these approaches is that they do not account for the influence of the ligaments as obstacles to diffusion [23]. Hence, unless the diffusion coefficient is treated as a fitting parameter (as done in Ref. [23]), this type of approach does not predict a decrease of the dealloying rate with the content of sacrificial element in the precursor alloy as observed experimentally [23,25].

In contrast, we consider here that LMD consists in the formation of two phases (solid ligaments and liquid channels) at the reaction layer and that the diffusion only occurs in the liquid phase. Accounting for the role of the solid ligaments impeding the diffusion enables to reproduce the expected increase of the dealloying rate with increasing content of sacrificial element in the precursor obtained experimentally. However, our analysis shows that considering the formation of two phases at the dealloying front leads to an infinite number of possible equilibria at the dealloying front and an infinite number of valid solutions to the diffusion problem. Measurements of phase fractions and compositions at the dealloying front reveals that the interfacial equilibrium can be selected from a maximum velocity criterion of the dealloying front (see Fig. 7).

A similar extremum criterion has been used in the context of eutectic solidification [36,44–47]. Both problems share similarities because eutectic solidification also consists in the growth of a two phase aggregate (both eutectic phases) in a parent phase (the liquid). As in the situation at hand, the equations for diffusion and mass conservation do not allow to solve for all the unknowns of the problem and an infinite number of solution are admissible. For isothermal solidification conditions (respectively for directional solidification), the velocity of the transformation front (resp. the front undercooling) depends on the lamellar spacing of the eutectic microstructure and exhibits a maximum (resp. a minimum) at a specific spacing [36,44]. Considering this extremum as the operating point of the eutectic solidification process was rationalized by the means of linear stability analysis showing the destabilization of larger spacings [46]. In addition, the lamellar spacing predicted by this criterion was shown to compare well with experimental observations [47]. In this study, maximizing the interface velocity remains a phenomenological criterion allowing to reproduce the experimental results. A more thorough and physically-based justification of this criterion is left as a prospect of this work.

Another debatable assumption of the numerical model developed in Section 4.2 consists in considering that the liquid channels and the solid ligaments are both at equilibrium in the dealloyed region. Including this effect is necessary to reproduce the composition gradients in the solid ligaments and the evolution of the liquid fraction in the dealloyed layer. However, the compositions measured experimentally show that both liquid and solid phases are not at equilibrium. To show more clearly this discrepancy, Fig. 13 reports EDX measurements of solid and liquid compositions at different positions of the dealloyed layer in the NiCuAg ternary phase diagram. Even if wide uncertainties are associated with these experimental measurements – in particular in the liquid where the compositions are obtained indirectly – the reported compositions are significantly away from tie-lines, suggesting that solid and liquid are not at equilibrium. This is attributed to the diffusion process associated to this composition change: reaching an equilibrium requires the diffusion of Cu across the width of the ligaments. Considering a ligament width of 1 μm (estimated from Fig. 3) and a solid-state diffusion coefficient $D_s = 4 \times 10^{-14}$ m^2/s [48], the characteristic diffusion time $t_d = 25$ s is comparable to the dealloying time used in experiments. Therefore, considering an instantaneous equilibrium

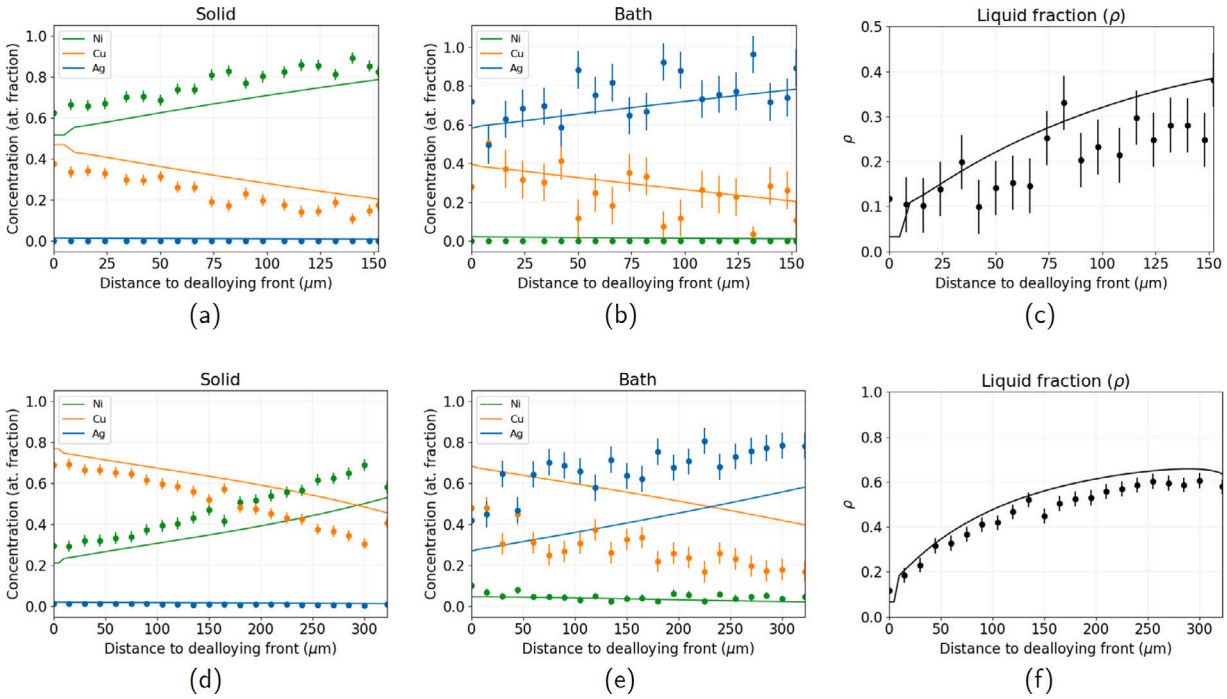

Fig. 12. Composition (solid ligaments and liquid channels) and liquid fraction profiles for dealloyed precursors $Ni_{50}Cu_{50}$ (top) and $Ni_{20}Cu_{80}$ (bottom) at 1000 °C. Error bars for the experimental composition profiles represent the standard deviation away from a linear fit. The error bars for ρ correspond to the standard deviation of the difference between experimental and numerical results.

between both phases appears like an over-simplifying assumption that should only be considered valid for very long dealloying times. For the dealloying times considered here, the change in composition of the liquid channels serves as a changing boundary condition triggering the diffusion of Cu across the solid ligaments. This explanation is consistent with the offset observed in Fig. 13: at a specific position of the dealloyed layer, the amount of Cu in the liquid decreases continuously with time because of the stretching of the composition gradient in the liquid channels. Because of the characteristic time associated to the solid-state diffusion of Cu across the ligaments, the amount of Cu in the ligaments is higher than predicted by the equilibrium with the liquid phase.

7. Conclusion

In this work, we propose a 1D diffusion model to simulate the dealloying reaction of NiCu alloys in an Ag bath. Parameterized with the thermodynamic data and diffusion coefficients of this system, the model's results are successfully compared to experimental measurements. The main findings are summarized as follows:

1. Comparing the prediction of simplified analytical models with experimental measurements reveals that properties of the dealloying front (compositions and fractions of phases) are well reproduced by the model if a maximum velocity criterion is considered.
2. Based on this criterion, the numerical model presented here predicts an increase of the dealloying rate for precursors with higher amounts of sacrificial element, which is consistent with experiments measurements.
3. In accordance with previous phase field results [14], the diffusion model predicts an increase of the interface liquid composition of the sacrificial element. This increase is a direct consequence of the maximum velocity criterion and depends on the thermodynamic data (i.e. on the shape of the phase diagram).

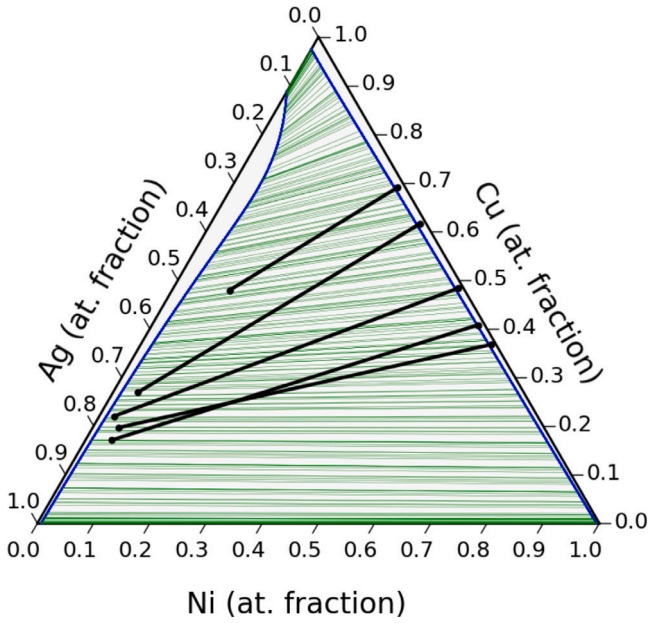

Fig. 13. Compositions measured experimentally for ligaments and liquid channels in the dealloyed region in dealloying of $Ni_{20}Cu_{80}$ at 1000 °C for 100 s (black lines) compared to equilibrium conditions predicted by the NiCuAg ternary phase diagram (green tie-lines) [17]. Error bars are not displayed for the sake of readability but are similar to that from Fig. 12. (For interpretation of the references to colour in this figure legend, the reader is referred to the web version of this article.)

4. The model also reproduces satisfactorily the composition profiles observed in both solid and liquid phases in the dealloyed region. The discrepancies observed between numerical and experimental results are attributed to the time required for solid-state diffusion within the ligaments.

To achieve a better agreement between numerical results and experimental measurements, it seems desirable to incorporate the influence of lateral diffusion in the ligaments across the dealloyed region. This could be achieved by solving 1D diffusion problems associated to the lateral diffusion of Cu across the solid ligaments. The composition in the liquid would be used as a time-dependent boundary condition for this diffusion problem. Solving this lateral diffusion problem at every position of the dealloyed layer would certainly improve the agreement between the numerical results and the composition profiles measured experimentally.

The present work focuses on the dealloying of NiCu alloys in pure Ag melt. It is considered as a model system for LMD because the associated phase diagram is fairly simple and has been well assessed in previous works [17]. It would be valuable to apply the model to other systems, such as TaTi dealloyed in Cu melt that has been investigated experimentally [23,49] and modelled with phase field approaches [13,14]. The phase diagram of TaTiCu at high temperatures is comparable to the one of NiCuAg [14], such that the findings reported here should also apply to this system. Investigating the transferability of the model to systems presenting more complex phase diagrams would also be of great interest. Indeed, Mg is an interesting dealloying agent because its melting temperature is low and it is immiscible with several metals (Fe, Cr, Mo, Ti, Mn, Ta, etc.) to the notable exception of Ni and Cu. Combining these elements allows to elaborate various precursors (e.g. FeNi or TiCu) easily dealloyable in Mg to obtain porous structures of the desired compositions [9,42,50–52], including high entropy alloys [12,53,54] and intermetallic compounds [2]. However, the phase diagrams associated to these systems can be more complex than the one considered here and include stoichiometric phases and ternary equilibria (see e.g. [55] for the FeNiMg system). Adapting the diffusion model to these cases therefore appears as a desirable prospect of this work. It could clarify the role of intermetallic phases on (i) the equilibria on the dealloying front, (ii) the kinetics of the dealloying process and (iii) the composition and microstructure gradients emerging from the LMD process. In summary, the diffusion model developed here paves the way to a predictive modelling of the dealloying kinetics and of the resulting microstructures on length and time scales compatible with experimental ones on a wide variety of systems.

CRediT authorship contribution statement

Louis Lesage: Formal analysis, Investigation, Methodology, Software, Visualization, Writing – original draft, Conceptualization. **Takumi Suga:** Investigation, Methodology. **Takeshi Wada:** Conceptualization, Supervision, Writing – review & editing. **Hidemi Kato:** Supervision, Writing – review & editing, Project administration. **Christophe Le Bourlot:** Supervision, Writing – review & editing. **Eric Maire:** Supervision, Writing – review & editing. **Nicolas Mary:** Conceptualization, Funding acquisition, Project administration, Supervision, Writing – review & editing. **Pierre-Antoine Geslin:** Conceptualization, Funding acquisition, Investigation, Methodology, Project administration, Supervision, Validation, Writing – original draft, Writing – review & editing.

Declaration of competing interest

The authors declare that they have no known competing financial interests or personal relationships that could have appeared to influence the work reported in this paper.

Acknowledgements

The authors acknowledge the support of the EPOPEE project by LABEX MANUTECH-SISE (ANR-10-LABX-0075) at Université de Lyon, within the framework of the Plan France 2030 operated by the French National Research Agency (ANR). The authors acknowledge the support of ELyT Global LIA for travel expenses.

References

[1] Y. Ding, M. Chen, Nanoporous metals for catalytic and optical applications, MRS Bull. 34 (8) (2009) 569–576.
[2] R. Song, J. Han, M. Okugawa, R. Belosludov, T. Wada, J. Jiang, D. Wei, A. Kudo, Y. Tian, M. Chen, et al., Ultrafine nanoporous intermetallic catalysts by high-temperature liquid metal dealloying for electrochemical hydrogen production, Nature Commun. 13 (1) (2022) 5157.
[3] Z. Wang, J. Liu, C. Qin, H. Yu, X. Xia, C. Wang, Y. Zhang, Q. Hu, W. Zhao, Dealloying of Cu-based metallic glasses in acidic solutions: products and energy storage applications, Nanomaterials 5 (2) (2015) 697–721.
[4] Y. An, Y. Tian, C. Wei, Y. Tao, B. Xi, S. Xiong, J. Feng, Y. Qian, Dealloying: An effective method for scalable fabrication of 0D, 1D, 2D, 3D materials and its application in energy storage, Nano Today 37 (2021) 101094.
[5] H.W. Pickering, Characteristic features of alloy polarization curves, Corros. Sci. 23 (10) (1983) 1107–1120.
[6] J. Erlebacher, M.J. Aziz, A. Karma, N. Dimitrov, K. Sieradzki, Evolution of nanoporosity in dealloying, Nature 410 (6827) (2001) 450–453.
[7] Y. Sun, Y. Ren, New preparation method of porous copper powder through vacuum dealloying, Vacuum 122 (2015) 215–217.
[8] X. Liu, A. Ronne, L.-C. Yu, Y. Liu, M. Ge, C.-H. Lin, B. Layne, P. Halstenberg, D.S. Maltsev, A.S. Ivanov, et al., Formation of three-dimensional bicontinuous structures via molten salt dealloying studied in real-time by in situ synchrotron X-ray nano-tomography, Nature Commun. 12 (1) (2021) 3441.
[9] T. Wada, K. Yubuta, A. Inoue, H. Kato, Dealloying by metallic melt, Mater. Lett. 65 (7) (2011) 1076–1078.
[10] M. Tsuda, T. Wada, H. Kato, Kinetics of formation and coarsening of nanoporous α-titanium dealloyed with Mg melt, J. Appl. Phys. 114 (11) (2013).
[11] P.-A. Geslin, M. Buchet, T. Wada, H. Kato, Phase-field investigation of the coarsening of porous structures by surface diffusion, Phys. Rev. Mater. 3 (8) (2019) 083401.
[12] T. Wada, P.-A. Geslin, D. Wei, H. Kato, Partial liquid metal dealloying to synthesize nickel-containing porous and composite ferrous and high-entropy alloys, Commun. Mater. 4 (1) (2023) 43.
[13] P.-A. Geslin, I. McCue, B. Gaskey, J. Erlebacher, A. Karma, Topology-generating interfacial pattern formation during liquid metal dealloying, Nature Commun. 6 (1) (2015) 8887.
[14] L. Lai, P.-A. Geslin, A. Karma, Microstructural pattern formation during liquid metal dealloying: Phase-field simulations and theoretical analyses, Phys. Rev. Mater. 6 (9) (2022) 093803.
[15] L. Lai, B. Gaskey, A. Chuang, J. Erlebacher, A. Karma, Topological control of liquid-metal-dealloyed structures, Nature Commun. 13 (1) (2022) 2918.
[16] N. Bieberdorf, M. Asta, L. Capolungo, Grain boundary effects in high-temperature liquid-metal dealloying: a multi-phase field study, NPJ Comput. Mater. 9 (1) (2023) 127.
[17] X.J. Liu, F. Gao, C.P. Wang, K. Ishida, Thermodynamic assessments of the Ag-Ni binary and Ag–Cu-Ni ternary systems, J. Electron. Mater. 37 (2008) 210–217.
[18] I. Steinbach, B. Böttger, J. Eiken, N. Warnken, S. Fries, Calphad and phase-field modeling: a successful liaison, J. Phase Equilib. Diffus. 28 (2007) 101–106.
[19] A.A. Wheeler, W.J. Boettinger, G.B. McFadden, Phase-field model for isothermal phase transitions in binary alloys, Phys. Rev. A 45 (10) (1992) 7424.
[20] S.G. Kim, W.T. Kim, T. Suzuki, Phase-field model for binary alloys, Phys. Rev. E 60 (6) (1999) 7186.
[21] A. Karma, W.-J. Rappel, Quantitative phase-field modeling of dendritic growth in two and three dimensions, Phys. Rev. E 57 (4) (1998) 4323.
[22] W.J. Boettinger, J.A. Warren, C. Beckermann, A. Karma, Phase-field simulation of solidification, Annu. Rev. Mater. Res. 32 (1) (2002) 163–194.
[23] I. McCue, B. Gaskey, P.-A. Geslin, A. Karma, J. Erlebacher, Kinetics and morphological evolution of liquid metal dealloying, Acta Mater. 115 (2016) 10–23.
[24] M. Mokhtari, C. Le Bourlot, J. Adrien, A. Bonnin, W. Ludwig, P.-A. Geslin, T. Wada, J. Duchet-Rumeau, H. Kato, E. Maire, In situ observation of liquid metal dealloying and etching of porous FeCr by X-ray tomography and X-ray diffraction, Materialia 18 (2021) 101125.
[25] S.-H. Joo, T. Wada, H. Kato, Development of porous FeCo by liquid metal dealloying: Evolution of porous morphology and effect of interaction between ligaments and melt, Mater. Des. 180 (2019) 107908.
[26] M. Mokhtari, C. Le Bourlot, J. Adrien, S. Dancette, T. Wada, J. Duchet-Rumeau, H. Kato, E. Maire, Cold-rolling influence on microstructure and mechanical properties of NiCr-Ag composites and porous NiCr obtained by liquid metal dealloying, J. Alloys Compd. 707 (2017) 251–256.
[27] H.-T. Luo, S.-W. Chen, Phase equilibria of the ternary Ag–Cu-Ni system and the interfacial reactions in the Ag–Cu/Ni couples, J. Mater. Sci. 31 (1996) 5059–5067.
[28] S. an Mey, Thermodynamic re-evaluation of the CuNi system, CALPHAD 16 (3) (1992) 255–260.
[29] M. Singleton, P. Nash, The Ag-Ni (silver–nickel) system, J. Phase Equilib. 8 (2) (1987) 119–121.
[30] T. Yamamura, T. Ejima, Diffusion of monovalent solutes in liquid copper and silver, Japan Inst. Metals J. 37 (1973) 901–907.

[31] W. Boettinger, D. Shechtman, R. Schaefer, F. Biancaniello, The effect of rapid solidification velocity on the microstructure of Ag–Cu alloys, Metall. Trans. A 15 (1984) 55–66.
[32] I. Tuah-Poku, M. Dollar, T.B. Massalski, A study of the transient liquid phase bonding process applied to a Ag/Cu/Ag sandwich joint, Metall. Trans. A 19 (1988) 675–686.
[33] M. Tsuda, T. Wada, H. Kato, Kinetics of formation and coarsening of nanoporous α-titanium dealloyed with Mg melt, J. Appl. Phys. 114 (11) (2013).
[34] J.W. Kim, M. Tsuda, T. Wada, K. Yubuta, S.G. Kim, H. Kato, Optimizing niobium dealloying with metallic melt to fabricate porous structure for electrolytic capacitors, Acta Mater. 84 (2015) 497–505.
[35] I. McCue, E. Benn, B. Gaskey, J. Erlebacher, Dealloying and dealloyed materials, Annu. Rev. Mater. Res. 46 (2016) 263–286.
[36] J.A. Dantzig, M. Rappaz, Solidification, EPFL Press, 2009.
[37] C.N. Singman, Atomic volume and allotropy of the elements, J. Chem. Educ. 61 (2) (1984) 137.
[38] A. Berezhkovskii, M. Pustovoit, S. Bezrukov, Diffusion in a tube of varying cross section: Numerical study of reduction to effective one-dimensional description, J. Chem. Phys. 126 (13) (2007).
[39] M.H. Jacobs, M. Jacobs, Diffusion Processes, Springer, 1935.
[40] J.-O. Andersson, T. Helander, L. Höglund, P. Shi, B. Sundman, Thermo-calc & DICTRA, computational tools for materials science, CALPHAD 26 (2) (2002) 273–312.
[41] C. Zhao, T. Wada, V. De Andrade, G.J. Williams, J. Gelb, L. Li, J. Thieme, H. Kato, Y.-C.K. Chen-Wiegart, Three-dimensional morphological and chemical evolution of nanoporous stainless steel by liquid metal dealloying, ACS Appl. Mater. Interfaces 9 (39) (2017) 34172–34184.
[42] M. Mokhtari, C. Le Bourlot, J. Adrien, A. Bonnin, T. Wada, J. Duchet-Rumeau, H. Kato, E. Maire, Microstructure characterization by X-ray tomography and EBSD of porous FeCr produced by liquid metal dealloying, Mater. Charact. 144 (2018) 166–172.
[43] L. Shen, Z. Chen, Critical review of the impact of tortuosity on diffusion, Chem. Eng. Sci. 62 (14) (2007) 3748–3755.
[44] K. Jackson, J. Hunt, Lamellar and rod eutectic growth, in: Dynamics of Curved Fronts, Elsevier, 1988, pp. 363–376.
[45] W. Kurz, R. Trivedi, Eutectic growth under rapid solidification conditions, Metall. Trans. A 22 (1991) 3051–3057.
[46] V. Datye, J. Langer, Stability of thin lamellar eutectic growth, Phys. Rev. B 24 (8) (1981) 4155.
[47] R. Trivedi, J. Mason, J. Verhoeven, W. Kurz, Eutectic spacing selection in lead-based alloy systems, Metall. Trans. A 22 (1991) 2523–2533.
[48] Y. Iijima, K.-I. Hirano, M. Kikuchi, Determination of intrinsic diffusion coefficients in a wide concentration range of a Cu-Ni couple by the multiple markers method, Trans. Japan Inst. Metals 23 (1) (1982) 19–23.
[49] B. Gaskey, I. McCue, A. Chuang, J. Erlebacher, Self-assembled porous metal-intermetallic nanocomposites via liquid metal dealloying, Acta Mater. 164 (2019) 293–300.
[50] T. Wada, H. Kato, Three-dimensional open-cell macroporous iron, chromium and ferritic stainless steel, Scr. Mater. 68 (9) (2013) 723–726.
[51] A. Okulov, A. Volegov, I. Okulov, Dealloying-based metal-polymer composites for biomedical applications, Scr. Mater. 146 (2018) 290–294.
[52] I. Okulov, A. Okulov, I. Soldatov, B. Luthringer, R. Willumeit-Römer, T. Wada, H. Kato, J. Weissmüller, J. Markmann, Open porous dealloying-based biomaterials as a novel biomaterial platform, Mater. Sci. Eng. C 88 (2018) 95–103.
[53] A.V. Okulov, S.-H. Joo, H.S. Kim, H. Kato, I.V. Okulov, Nanoporous high-entropy alloy by liquid metal dealloying, Metals 10 (10) (2020) 1396.
[54] S.-H. Joo, J.W. Bae, W.-Y. Park, Y. Shimada, T. Wada, H.S. Kim, A. Takeuchi, T.J. Konno, H. Kato, I.V. Okulov, Beating thermal coarsening in nanoporous materials via high-entropy design, Adv. Mater. 32 (6) (2020) 1906160.
[55] P. Wang, J. Zhao, Y. Du, H. Xu, T. Gang, J. Fen, L. Zhang, C. He, S. Liu, H. Ouyang, Experimental investigation and thermodynamic calculation of the Fe-Mg-Mn and Fe-Mg-Ni systems, Int. J. Mater. Res. 102 (1) (2011) 6–16.